Structural and Electrochemical Characterization of $NdBa_{1-x}Co_{2-y}Fe_yO_{5+\delta}$ as Cathode for Intermediate Temperature Solid Oxide Fuel Cells

Giulio Cordaro[a,b,z], *Alessandro Donazzi*[b,z], *Renato Pelosato*[a,c], *Luca Mastropasqua*[b], *Cinzia Cristiani*[a], *Isabella Natali Sora*[c], *Giovanni Dotelli*[a]

[a]Politecnico di Milano, Dipartimento di Chimica Materiali e Ingegneria Chimica "G. Natta", Piazza Leonardo da Vinci 32, 20133 Milano, Italy, [b]Dipartimento di Energia, Politecnico di Milano, Via Lambruschini 4, 20156 Milano Italy, [c]INSTM R.U. and Università di Bergamo, Dipartimento di Ingegneria, Viale Marconi 5, 24044 Dalmine
[z]Corresponding Author E-mail Address [giulio.cordaro@polimi.it]

Keywords: Layered Perovskite, IT-SOFC, Cathode, EIS, ECM, DRT

Abstract

$NdBa_{1-x}Co_{2-y}Fe_yO_{5+\delta}$ (NBCFd) layered perovskites are investigated as cathodes in Intermediate Temperature Solid Oxide Fuel Cells. The effects of Fe doping (up to 20%) and Ba deficiency (up to 10%) are explored. The compounds are prepared via molten citrate route and characterized by XRPD, SEM, TGA and cerimetric titration. The electrochemical properties are tested via 4-probe conductivity measurement and impedance experiments on symmetric cells at varying temperature (550-700°C) and O_2 pressure (5-100% v/v). The compositional tailoring leads to activity variation and distinct oxygen reduction behavior. An ordered layered structure with tetragonal lattice (*P4/mmm*) is found, whose cell volume increases with Fe doping and decreases with Ba deficiency. High total conductivity (150-450 S/cm at 700°C) is measured despite the hindering effect of Fe. In stoichiometric compounds, Fe doping reduces the polarization resistance, while an increase is observed in Ba-deficient samples. The impedance results are rationalized by distribution of relaxation times analysis and equivalent circuit modeling, which reveal that the steps of surface electronation and ion transfer across the electrode/electrolyte interface are determining. Acting on electronation, Fe doping influences the electrode's activity. The target performance for application is achieved at 10% Ba deficiency and 5% Fe doping (0.14 $\Omega \cdot cm^2$ at 700°C).

Introduction

Layered perovskites are a class of solid oxides composed by the alternation of the ABO_3 and $A'BO_3$ single perovskite structures along the *c*-axis. The general formula is $AA'B_2O_{5+\delta}$ and the regular alternation of A-O, B-O and A'-O, B-O layers is governed by the difference in ionic radii between the A and A' elements. This structural order is typically obtained with a rare earth element and an alkaline earth in the A and A' site respectively, while the B site is occupied by a transition metal, frequently cobalt. Layered perovskites based on cobalt have received increasing consideration due to the high concentration of oxygen vacancies that can

be stabilized in the lattice (even δ below 0.5), exhibiting at the same time high electronic conductivity and catalytic activity towards the Oxygen Reduction Reaction (ORR) [1]. This class of compounds is suitable for application as cathodic materials in IT-SOFCs, but further investigation is necessary to improve their stability without hampering the electrochemical activity [2]. Very recent works were focused on the characterization of layered perovskites with neodymium in A site in order to improve the performances through doping or substitutions of A' cations with Sr [3, 4], Ca [5] or both [6, 7], and B cations with Cu [5], Mn [8]or Zr [9].
Recently, the improvement of the electrochemical activity through the introduction of Ba deficiency was demonstrated for several layered perovskite structures [10-15]. In our previous work [15], we showed that a small Ba understoichiometry in $NdBaCo_2O_{5+\delta}$ is beneficial for the performance of the cathode. To reduce thermal stresses and increase long-term stability, the substitution of Co with Fe is reported to be a valid option. Cherepanov et al. [16] observed a great reduction of Thermal Expansion Coefficient (TEC) by substituting Co with Fe in the Nd-based layered perovskite. However, the introduction of large amounts of Fe drastically reduced the cathodic efficiency [17-22], while keeping the doping to a small extent improved the performance of the Pr-based layered cobaltite [23]. Lately, molecular dynamics simulations performed on similar compositions suggested that iron doping promotes oxygen ions diffusivity, up to a cobalt substitution of 25% [24].

In this work, the effect of Fe doping on $NdBaCo_2O_{5+\delta}$ was investigated in compounds with and without Ba understoichiometry. The NBCF series ($NdBaCo_{2-y}Fe_yO_{5+\delta}$ with y = 0, 0.1, 0.2, 0.3, 0.4) and the NBCFd series ($NdBa_{0.9}Co_{2-y}Fe_yO_{5+\delta}$ with y = 0, 0.1, 0.4) were characterized. The aim of this work is to evaluate if the introduction of both Ba understoichiometry and Fe doping provides advantages in terms of performance.

Experimental

Synthesis procedure

All the compounds were synthesized via the molten citrate technique that allows to achieve a fine powder microstructure, typical of wet synthesis procedures, at lower temperature than conventional synthesis. Proper amounts of $Nd(NO_3)_3 \cdot 6H_2O$, $Ba(NO_3)_2$, $Co(NO_3)_2 \cdot 6H_2O$ and $Fe(NO_3)_3 \cdot 9H_2O$ (Sigma-Aldrich) were dissolved in distilled water and citric acid monohydrate ($C_6H_8O_7 \cdot H_2O$) was added in excess to ensure the complete cations chelation. The molar ratio of citric acid and metal cations was fixed at 7. The obtained solution was heated up to 140°C under vigorous stirring until complete decomposition of the nitrates and formation of a dark purple viscous slurry. Subsequently, the slurry was treated in oven at 360°C for 5 hours, then ground and calcined at 1100°C for 10 hours, with heating and cooling ramps of 5°C/min.

Structural characterization

The powders were then ground again and analyzed with X-Ray Powder Diffraction (XRPD) technique with a Bruker D8 Advance Diffractometer with Cu-Kα radiation and graphite

monochromator. The diffraction patterns were collected in the range 20-80° 2θ with a 0.02 step and 12 seconds of counting time and Rietveld refinements of the structures were performed using the GSAS software [25]. Thermogravimetric Analyses (TGA) were carried out on all samples with a simultaneous TG-DTG Seiko 6300 instrument. The compounds were heated from room temperature to 850°C at 3°C/min and the weight variations were correlated to their oxygen content. The oxygen content of the compounds at room temperature was estimated by cerimetric redox titrations. The complete reduction of Co^{n+} and Fe^{n+} to Co^{2+} and Fe^{2+} was obtained using a known excess of $FeCl_2$, that was back-titrated with $Ce(SO_4)_2$, using ferroin as indicator. The molar amount of reacted $Ce(SO_4)_2$ directly corresponds to the molar amount of $FeCl_2$ required to completely reduce Co and Fe cations in the NBCFd compounds. The average oxidation state of the B site could then be calculated according to stoichiometric relations. For each sample, the procedure was repeated three times and the results averaged. More detailed information can be found in our previous work [15].

Electrochemical characterization

The conductivity and polarization resistance measurements were carried out with a potentiostat/galvanostat (AMEL 7050) equipped with a Frequency Response Analyzer (520 FRA Materials Mates). The electrical conductivity was measured between 25 and 750°C with a four-electrode probe method on sintered bars (25 mm long, 5 mm wide, 3 mm thick, sintered in air at 1100°C for 4 h). The calcination temperature of the bars was purposely kept at 1100°C, in order for the samples to be representative of the cell electrodes and to avoid Co volatilization, even if a complete densification of the bars was not attained at that temperature. The measured values of conductivity were then normalized by the solid fraction of the bar, which is the complementary of the porosity value [26]. The porosity of the bars was calculated as the ratio between the relative and theoretical density of the bars. The relative density was measured with the buoyancy balance in ethanol, while the theoretical one was calculated from the lattice parameters obtained in the Rietveld analysis.

Furthermore, EIS tests were performed on a GDC ($Ce_{0.9}Gd_{0.1}O_{2-\delta}$) electrolyte-supported cell with symmetrical porous layers on both sides. The pellets were prepared via die pressing at 1 ton for 7 minutes using a 16 mm die, followed by sintering at 1500°C for 6 hours in air. The diameter of the sintered pellets was 11 mm, with a thickness of 1 mm. The relative density was higher than 97%. The cathode layer was deposited on each side with an ink made of 60% w/w of powders and 40% of a slurry composed by terpineol, isopropyl alcohol and ethyl cellulose in weight ratio 76:20:4. The cathode layers were dried at 120°C for 6 hours and then calcined at 1100°C for 10 hours to achieve good adhesion. The porosity of the electrodes was measured with mercury porosimetry and resulted equal to 40% for all the samples. The measured weight of the electrodes allowed to calculate the thickness, based on the theoretical density. The values are reported in Table S1 of the Supporting Information file. At the top of each cathode, silver meshes were applied as current collectors, painted with Ag ink to guarantee long-lasting contact between mesh and electrode during the EIS measurements. For each sample, the EIS tests were carried out between 750°C and 550°C, at OCV with 10 mV voltage amplitude in the 0.1 Hz – 10 kHz frequency range. At each temperature, the measurements were performed under 50 Ncc/min flow varying the oxygen

partial pressure in nitrogen at 5%, 10%, 21% (air flow) and 100% (pure O_2). Systematic control of the effect of mass diffusion limitation was performed varying the diluent from N_2 to He, with same oxygen content. In addition, the morphological features of the calcined powders and of the electrodes of the symmetric cells were assessed via Scanning Electron Microscopy (SEM) using a Cambridge Stereoscan 360.

Data modelling

The deconvolution of EIS spectra was performed using the Distribution of Relaxation Time (DRT) analysis tool proposed by Saccoccio et al. [27], which implements the Tikhonov regularization method into an online tool with graphic user interface. Finally, the Equivalent Circuit Model (ECM) was used to fit the EIS spectra results and estimate the different polarization contributions present in the spectra. The aim was to distinguish between physical, chemical and electrochemical processes occurring during the ORR at the cathode, in order to identify the rate determining step of the global reaction and investigate the relationship with crystalline structure and electrical properties.

Results

Structural Characterization

The names and formula of the compounds are summarized in Table 1, together with crystal structure information. Figure 1 reports the XRPD spectra of all the samples after the final calcination step at 1100°C. All the compounds could be indexed in an A-site ordered structure with regular alternation of $Nd(Co,Fe)O_3$-$Ba(Co,Fe)O_3$ simple perovskite units. The analysis of the XRPD patterns allowed to identify low amounts of $NdCoO_3$ (PDF #00-025-1064) impurity phase in the understoichiometric samples NBCd, NBCFd1 and NBCFd4. Other small impurity peaks could be detected in samples NBCF1 ($BaCoO_{2.93}$ - PDF #00-026-0144 - and Nd_2O_3 - PDF #00-006-0408) and traces of $BaFeO_{3-x}$ (PDF #00-023-1024) in NBCF2 and NBCF4 [28]. The impurity amounts were quantified with Rietveld refinement routines and the highest values were found for $NdCoO_3$ in the NBCFd1 and NBCFd4 samples. The mass fraction of $NdCoO_3$ resulted equal to 1.6% and 4.7% respectively. The other impurities were too small to lead to consistent calculations in the Rietveld routine, and then considered negligible.

Structural Effects of Compositional Modifications

The introduction of iron in the structure triggers a modification of the pristine orthorhombic lattice cell of NBC (space group *Pmmm*, n° 47) [15] to a tetragonal one (space group *P4/mmm*, n° 123) for NBCF and NBCFd compounds. For what attains to the cell size, the cell volume increases with Fe doping, both in the stoichiometric compounds and in the Ba deficient ones. This is mainly due to the variation of the *c* lattice parameter, which increases

from 7.615 Å for NBCF1 to 7.645 Å NBCF4, and from 7.614 Å for NBCFd1 to 7.650 Å NBCFd4. These values are in agreement with literature data reported by Cherepanov et al. for $NdBaCo_{2-x}Fe_xO_{5+\delta}$ with x = 0, 0.2, 0.4 [16] and by Kim et al. for samples with x = 0 and 0.5 [18]. The introduction of Ba deficiency instead, affects the lattice size in the opposite way, slightly decreasing cell volumes (compare the lattice parameters of sample NBC with the ones of NBCd, those of NBCF1 with the one of NBCFd1, and NBCF4 with NBCFd4). The variation of the cell volume is related to the ionic size of Co^{n+} in different oxidation states, 0.53/0.61/0.745 Å for $Co^{2+}/Co^{3+}/Co^{4+}$ respectively, in a six-fold coordination [29].

Oxygen content

As Nd and Ba cations have a fixed oxidation state (Nd^{3+} and Ba^{2+}), the oxygen content in the compounds examined is only due to the average oxidation state of B site cations, i.e., Co and Fe [30]. In general, at room temperature, the average oxidation state of Co and Fe in a compound reflects the cell size behavior because of the amount of oxygen they are bound to, expressed in the formula as 5+δ. Moreover, Co/Fe oxidation state (and therefore the amount of oxygen) also depends on the thermal history of the sample, that is, on the time it takes for the lattice oxygen to equilibrate with the external atmosphere during the phase formation and the following cooling ramp (i.e., on the heating and cooling rates). The cerimetric titrations allow measuring the average oxidation state of B cations, and therefore the total oxygen content of compounds. The trend observed in the total oxygen content at room temperature is well related with the measured lattice volumes: the oxygen content increases with increasing Fe content and decreases with increasing Ba deficiency. The same happens for the lattice volumes. The increase of oxygen content observed when increasing Fe doping can be explained by the higher strength of the Fe-O bond compared to the Co-O bond [16]. Thus, oxygen vacancies preferentially form at the oxygen sites bound to cobalt. When part of cobalt is substituted by iron, the maximum extent of oxidation is reduced. It is interesting to note that, on the one hand, the introduction of Fe enhances the number of oxygen vacancies in Ba deficient compounds while, on the other hand, it reduces the effect on the lattice volume. This is witnessed by the small change of the *c* parameter for Fe doping equal to 0.1, which becomes very important for Fe = 0.4, reaching the highest value for NBCFd4. Together with the lowest cell volume, NBCFd1 sample showed also the lowest oxygen content at room temperature, equal about to 5.51(5).

The variation of the oxygen content as a function of temperature is analyzed by means of TGA measurements (Fig. 2a-b), where the weight changes due to the exchange of oxygen between crystal lattice and air. All the samples show a similar trend, with a weight gain up to about 300°C and a weight loss from that temperature on. This observation is in agreement with the available literature results for this class of compounds [17, 18, 20, 22, 31]. From a structural viewpoint, oxygen loss preferentially occurs for oxygen atoms in position O2 (0, 0, 0.5) in the crystal model used for Rietveld refinement [32]. However, it is reasonable to assume that Ba deficiency introduces oxygen vacancies in the proximity of the Ba cages. These vacancies influence the ability to release additional oxygen, as noted from the different slopes of the TGA curves (e.g., a steeper slope is found in the case of the NBCd compound compared to

NBC). The origin of the peculiar behavior of the 5+d oxygen content in deficient compounds is probably motivated by the preferential position of the vacancies, as a consequence of Ba understoichiometry. Generally, in layered perovskite based on Co, the oxygen vacancies are located in Co-O apical position, and the substitution of Co by Fe typically allows to stabilize higher amounts of oxygen in the Nd-Co-O planes. A possible explanation is that the presence of Ba deficiency together with the small amount of Fe doping (1 Fe cation every 19 Co) does not allow the stronger Fe-O bonds to show their effect, while, at the same time, the structure requires to release oxygen for stabilizing the presence of a slightly bigger cation.

Electrical Conductivity

The results of the electrical conductivity measurements as a function of temperature are reported in Fig. 2c-d. Close similarity is found between the conductivity curves and the TGA curves. Both the slopes and the maxima in TGA plots (Fig. 2a-b) well agree with the ones in the conductivity curves; below roughly 300°C a semiconductor type mechanism is active, while above, a metallic-like behavior is observed for all the samples. The similarity of the two measurements is caused by the mechanism of oxygen exchange between the atmosphere and the lattice, which also affects the electron holes (that carry the electronic charge). The equilibria are expressed in Kröger-Vink notation [33] as follows:

$$2Co_{Co}^{\bullet} + O_O^x \leftrightarrow \frac{1}{2}O_2 + 2Co_{Co}^x + V_O^{\bullet\bullet}$$

$$2Fe_{Co}^{\bullet} + O_O^x \leftrightarrow \frac{1}{2}O_2 + 2Fe_{Co}^x + V_O^{\bullet\bullet}$$

In the equation, the reduction of Co ions (positive charge carriers, $Co_{Co}^{\bullet}$) at the expenses of lattice oxygen ions (O_O^x) generates molecular oxygen, oxygen vacancies ($V_O^{\bullet\bullet}$) and Co ions with no surplus charge. In agreement with literature reports [17, 18, 22, 23, 34], when cobalt is partially substituted with iron, lower conductivities are measured. However, the drop is not strictly linear with the iron content: the conductivity steadily decreases passing from the NBCF2 to the NBCF4 sample, whose conductivity is however comparable to the NBCF1 sample. The local minimum in the conductivity trend observed for y = 0.1 is similarly found in literature for analogous compositions of layered perovskites [23, 35]. In the case of Ba deficient compounds, NBCFd1 shows higher conductivity than NBCFd4, coherently with the increased amount of Fe and in contrast to the oxygen content. This behavior is probably related to the preferential formation of Fe^{4+}over Co^{4+}, for electronic charge compensation. Thus, since Fe^{4+}-O bonds are less covalent than Co^{4+}-O ones, electron localization increases and the conductivity decreases [36].

Nevertheless, the conductivity of NBCF4 in the IT-SOFC operating range (from 240 S/cm at 500°C to 149 S/cm at 750°C) is well above the target of 100 S/cm for cathode materials, which has been proposed as the limit to ensure negligible electrical resistance contributions by the electrode [37].

EIS Results

The EIS measurements were carried out on symmetrical NBCFd/GDC/NBCFd button cells. The choice of GDC as electrolyte material was made after a reaction test reported in the previous work on NBC compounds [15]. In order to verify the compatibility of the electrolyte material, the absence of reaction between electrolyte and cathode material was verified again for NBCFd series. A mixture of equal quantities of NBCFd4 and GDC was heated up to 1100°C for 10 hours and analyzed by XRPD. The spectra did not show any additional peak (Fig. S1 in the Supplementary Material document) and confirmed the stability of the phases even at high temperature. Fig. 3 reports a SEM image of the symmetrical cell used for the EIS tests of NBCFd1. The porous layer was deposited on the top of the dense electrolyte. SEM pictures showed good adhesion of the cathode layer with a thickness of about 15-20 µm for every cell (panel a). The morphology of the powders after calcination at 1100°C revealed good homogeneity of the grains, with the size of 1-2 µm (panel b) and agglomerates with different shapes due to the sintering process. The SEM images collected for the NBCFd1 sample are representative of all the other compounds. In Fig. 4, the Area Specific Resistance (ASR) values of the NBCFd series are presented in the Arrhenius plot. The ASR values are calculated as the ratio of the polarization resistance (R_{pol}) over the cathode area and divided by 2, due to the symmetric configuration of the cell ($R_{pol}/A/2$). The effect of Fe doping is highlighted in panels a and b: Fe doping reduces the polarization resistance R_{pol} for stoichiometric compounds (panel a), while it increases R_{pol} for compounds with Ba deficiency (panel b). The best performance of this series is obtained with NBCFd1, which shows slightly higher ASR values compared to NBCd (0.10 Ω·cm^2 at 700°C) [15], which is also reported in the plot. The ASR value of NBCFd1 at 700°C is equal to 0.14 Ω·cm^2, which makes this compound promising as cathode for IT-SOFCs. This result is very interesting considering that, compared to the more efficient NBCd compound, the substitution of Co with Fe should improve long-term stability.

The effect of Fe doping for the NBCFd series is shown in Fig. 4c on the ASR at 600°C and Fig. 4d on the apparent activation energy (E_{ACT}) derived from the ASR results in air. The increase of Fe content reduces the ASR values for stoichiometric compounds (x = 0) and the lowest value is found for NBCF4. This result is in line with the work of Zhang et al. [22], who also report an improvement of the performance for x = 0.3 and 0.4 in the series $PrBa_{0.5}Sr_{0.5}Co_{2-x}Fe_xO_{5+\delta}$. These authors find the smallest ASR value at 0.4 and observe a sharp increase for x = 0.5. In the $PrBaCo_{2-x}Fe_xO_{5+\delta}$ series, Zou et al. [23] obtain the best performance for the compound with x = 0.4, with ASR values almost half compared to the x = 0.2 sample. Upon increasing the Fe content, these authors report a constant increase, starting from x = 0.6 up to x = 2. The increase of ASR at high Fe contents is well known, although for x = 0.5 Kim et al. [18] report a reduction compared to the iron-free compound in the $NdBaCo_{2-x}Fe_xO_{5+\delta}$ series. With respect to smaller levels of Fe doping, as those explored in the present work, Tsvetkova et al. [38] observe a worse activity for $GdBaCo_{1.8}Fe_{0.2}O_{5+\delta}$ compared to the corresponding iron-free sample.

The ASR results also show that the introduction of Fe in the Ba deficient compounds increases the ASR values. However, it is important to note that NBCFd has a resistance one order of magnitude lower than NBC. For the y = 0.1 compound, the ASR reduction due to Ba deficiency is less pronounced but still significant. Instead, for the y = 0.4 compound, the Ba deficiency increases the ASR (Fig. 4c). The apparent activation energy (E_{ACT}) of the NBCFd

compounds ranges from 1.17 eV of the NBCFd1 and NBCF4 samples to 1.40 eV for NBCF1. A comparison E_{ACT} is reported as a function of the Fe doping in panel d of Fig. 4 for stoichiometric (blue lines) and deficient samples (red lines). Since the differences in E_{ACT} values are modest, almost identical evolution of the ASR as a function of the Fe content is found for every temperature. These values are similar to those found in literature for layered perovskites. Regarding $NdBaCo_{2-x}Fe_xO_{5+\delta}$, Kim et al. [18] obtained slightly higher values (1.45-1.80 eV), but it is probably related mainly to the different cell configuration and electrolyte material used for the measurements (LSGM electrolyte-supported cells with symmetrical interlayers of 1:1 LSGM + cathode mixture and cathode layers on top). Fe doping produces opposite results on ASR and E_{ACT} for stoichiometric and deficient series of compounds. This effect suggests that different contributions are involved in the overall ORR process. The shape of the spectra in the Nyquist plots confirms the occurrence of distinct simultaneous processes, especially visible at high temperature. In Fig. 5, the EIS results obtained for the NBCFd1 sample are reported for each temperature and oxygen partial pressure. The arcs appear as depressed semicircles with similar shapes at different operating conditions. Upon decreasing the O_2 partial pressure, the shape is retained at all the temperature levels, except of the additional arc at low frequencies, which appears at 700°C and 5% O_2 and which is related to gas diffusion. At 600°C and 550°C, a linear branch emerges at high frequencies. This is a typical indication of ionic diffusion limitation and it is often measured in MIEC materials [39]. The mixed conductivity allows extending the active surface of the electrode from the triple phase boundary to the entire cathodic surface. However, lowering the temperature, the ability of diffuse oxygen ions inside the bulk is hampered and starts to be a relevant contribution to the resistance of the global process. In Fig. 5, the results of fitting with ECM technique are also reported. The fitting outputs match very well the experimental data and allow obtaining information about the main steps of the process (Section 4.2). These measurements and the ECM fitting were performed for each sample of the NBCFd series, but the results are reported only for NBCFd1 due to its superior performance. These results are representative also of the other materials (Fig. S2-S5 in the Supplementary Material).

Quantification of the EIS spectra

The EIS tests were performed also using He as diluent instead of N_2 to evaluate the gas diffusion contribution. As shown in Fig. 5a, at low oxygen partial pressure (5%) a reduction in the polarization resistance is evident but still limited (from 0.27 to 0.22 $\Omega \cdot cm^2$ at 700°C), while in the case of the experiments in air the difference is negligible (not reported). This demonstrates that the EIS measurements collected are representative of resistance contributions intrinsically related to the kinetics of the electrochemical reactions.

DRT and ECM techniques were applied to analyze the EIS results. The application of DRT provides consistent indications on the number of the phenomena contributing to the measured EIS arcs. This result is the starting point for the ECM analysis, since it suggests the number of resistive elements to be selected in the equivalent circuit. After establishing the circuit, the parameters obtained by fitting the curves are examined as a function of

temperature and oxygen partial pressure, in order to calculate the activation energy (E_{ACT}) and the reaction order (α) of each process. From these values, it is possible to obtain a quantification of the main characteristic parameters describing the single reaction steps. In the following paragraphs, the results of these two analyses are reported in detail.

Distribution of Relaxation Times (DRT)

The DRT technique was exploited to deconvolute the EIS spectra into the frequency domain without any *a priori* assumption. A Tikhonov regularization method was implemented into the online tool with graphic user interface [27]. A discretization function was employed to approximate the function $Z(\omega_i)$ by minimizing the error function between the measured data and the discretization function employed (i.e., piecewise linear). A regularization function was introduced and employed to minimize the presence of strong oscillations in the distribution of relaxation time function and it is dependent on the regularization parameter, λ. The determination of the appropriate value of the regularization parameter was characterized by a trade-off between having a smoother distribution function and better fit of the measured data with the chosen discretization function. Typically, increasing λ allows having fewer oscillations in the distribution of relaxation time function, but a smoother function may come at the price of more bias between the model and the experimental data. After several simulations, a value equal to 10^{-3} was selected as regularization parameter, λ. More details can be found in literature [40-42]. The application of this technique gives a semi-quantitative indication about the single processes convoluted together in the EIS spectra. The DRT analysis was performed on all the EIS data and evidenced the same common main trends. Fig. 6 reports the results obtained on the NBCFd1 sample for every temperature upon varying the oxygen content. This technique allowed identifying the number of phenomenological contributions simultaneously present in the EIS spectra, in order to select an adequate circuit for the ECM analyses. Each main contribution is represented in the DRT graphs by a peak at a specific frequency. The area subtended by each peak represents an estimate of the resistance value, but the investigation of resistances deconvolution was performed through the more reliable ECM technique. At all the temperatures, three peaks can be distinguished: one in low frequency range (1-10 Hz), a second one at middle frequencies (10^2-10^3 Hz) and a last one at high frequencies (> 10^3 Hz). At 700°C (panel a) and 650°C (panel b), the high frequency peak is only partially visible, but it grows to completion upon decreasing the temperature: at 600°C and 550°C it appears as a neat peak, centered around 5 kHz. This high frequency peak keeps constant with the oxygen partial pressure, suggesting that the associated phenomenon is related to the transport of oxide ions, either across the interface or by lattice diffusion. At this frequency range, usually the interface involved is the electrolyte-cathode contact area [14, 43-45]. With respect to the arcs at low and middle frequency, the increase of oxygen partial pressure reduces the peaks area and shifts the characteristic frequencies to higher values, in line with a promotion of the associated rate. At low frequencies, the contribution to the resistance is related to gas diffusion. The disappearance of the peak for pure oxygen and the constant height lowering the temperature both support this identification. The middle frequency peak grows at

reducing both the oxygen pressure and the temperature. In addition, the middle frequency peak shifts towards lower frequencies at lower temperature, meaning that the characteristic time increases, and the process slows down. These indications suggest that a kinetic reaction step is involved, possibly occurring at the gas/cathode interface, due to its close relationship with the O_2 pressure. The same considerations hold at all the temperatures. The intensity of the middle frequency peak, and therefore the polarization resistance, proportionally increases more than the intensity of the high frequency peak, suggesting that the activation energy is higher. Differently, the low frequency peak does not appear to change significantly, in accordance with the small activation energy of gas diffusive phenomena. As a matter of fact, the results of the DRT analysis suggest that the main contributions of the resistance are three at 700°C and 650°C, while the low frequency one becomes almost negligible (and almost masked by the middle frequency peak) below 600°C. This consideration provides preliminary indications about the simplest circuit to fit the spectra with the ECM. The fitting procedure was performed considering three elements to simulate the EIS arcs. The ECM results, discussed in the following paragraph, confirm the goodness of this initial choice.

ECM Results

Consistently with the indications of the DRT, the impedance spectra were analyzed based on a circuit of the type $LR_{Ohm}(R_{HF}Q_{HF})(R_{MF}Q_{MF})(R_{LF}Q_{LF})$. A sketch of the circuit is reported as an insert in panel a of Fig. 5. The element L is the inductance caused by the electrical equipment and wires, R_{Ohm} is the ohmic resistance mainly due to the electrolyte, while the three RQ elements are associated with the main processes that take place in the electrode. For layered perovskite cathodes, it is common to fit the EIS results with three RQ elements [14, 44, 46, 47]. The high frequency arc (HF) is associated to ionic transfer processes, such as the inclusion of oxygen ions within the bulk of the electrolyte across the cathode/electrolyte interface. The middle frequency arc (MF) is related to electrode processes, such as the dissociative adsorption of oxygen, the formation of adsorbed oxygen ions, or the surface diffusion of oxygen adatoms; the low frequency arc (LF) is due to mass diffusive transport processes, either internal (intra-porous) or external (across the interphase boundary layer).

The parameters obtained by fitting to the spectra of the NBCd1 sample are summarized in Tables 2 and 3. These tables contain the values of the circuit elements and the values of the calculated equivalent capacitances and relaxation frequencies. For each process, the relaxation frequencies increase with the temperature and show values close to those found with the DRT analysis. The *n* coefficient of the Constant Phase Elements (CPE) are constant as a function of temperature and oxygen content. This is consistent with the fact that *n* is a morphological parameter, independent of the operating conditions. The value of this parameter for an ideal structure is 1, while usually a lower value is found due to imperfections of the electrode layer. The variation of the *n* parameter between the HF and the MF contributions is due to the different interfaces where those processes take place, which have distinct morphologies. In the case of the LF element, the exponent is related to the simplified treatment of the diffusion arc, which should in principle be taken as a Warburg-type. For each process, the resistance values obtained from the deconvolution are

evaluated as a function of the temperature, in order to obtain the activation energy, and as a function of the oxygen partial pressure in order to evaluate the reaction order. These parameters are summarized in Fig. 7, where panels a-c report the resistances versus the oxygen partial pressure in logarithmic scale, while panel d reports Arrhenius plot of the resistance contributions measured in air. This latter plot allows estimating the activation energy of each step. With respect to the low frequency contribution, the association to a gas diffusion process is confirmed: indeed, it is almost independent from temperature variations ($E_{ACT} \approx 0$) and its reaction order is close to 1 (1.04-1.15). In addition, the equivalent capacitance values are too high (> 1 F/cm^2) to be representative of an electrochemical step. Comparable results are found in the literature for similar compounds [12, 14, 45, 47]. Regarding the middle frequency process, the reaction order with P_{O2} (α) is close to 0.25. This value suggests that a charge transfer process from the cathode surface to the electrode lattice is governing the contribution. The capacitance (≈ 10^{-2} F/cm^2) is also in line with this assumption [10, 45, 48, 49]. A step of surface electronation of an adsorbed oxygen atom (O*) with ion inclusion of an oxide ion in the lattice and formation of a surface free site (*) is typically associated with this reaction order and can be represented by the following stoichiometry:

$$O^* + 2e^- + V_O^{\bullet\bullet} \leftrightarrow O_O^x + *$$

The MF contribution is the most relevant process in terms of polarization resistance for every measurement and its activation energy is equal to 1.24 eV. The high frequency element shows a zero order dependency on oxygen partial pressure, confirming the DRT results, which reveal that the corresponding peak does not change upon dilution with oxygen. This is a clear indication that the associated process is an ionic oxygen transfer, taking place at the interface between cathode and electrolyte, according to the following stoichiometry:

$$O_{O,Cat}^x + V_{O,Ele}^{\bullet\bullet} \leftrightarrow O_{O,Ele}^x + V_{O,Cat}^{\bullet\bullet}$$

This HF process shows an E_{ACT} in air equal to 1.18 eV with capacitance values between 10^{-3} and 10^{-4} F/cm^2 in line with literature for similar double perovskites [14, 43-45].

Analogous DRT and ECM analyses were carried out on all the NBCF samples prepared and tested (the ECM results of other compounds are reported in Tables S2 – S9 in the Supplementary Material). The same equivalent circuit was maintained, the same reaction orders were found and identical associations were confirmed between the three arcs and the RQ elements. As a matter of fact, the numerical analyses allow to extract main activity indicators (polarization resistance, capacitance and activation energy of the HF and MF arcs) that serve as the basis of a quantitative comparison among the samples and provide better insight in the consequences of the compositional tailoring.

Discussion

The performance of the different materials is compared based on the polarization resistance, R_{POL}, the activation energy, E_{ACT}; the capacitance of the middle frequency arc, C_{MF}, and of the high frequency arc, C_{HF}. With respect to the HF and MF resistances, Fig. 8 summarizes the results of the ECM simulation for each compound at 600°C in air (panels a and b). The evolution of these curves is representative of the measurements at all the other temperatures, since the difference in E_{ACT} between MF and HF is small (Fig. 8c). Panel a

reports the resistances of the high frequency process, which is identified as an ionic transfer at the cathode-electrolyte interface, while panel b reports the resistances of the middle frequency process, associated with electronation and ion inclusion. In the case of the stoichiometric compounds, Fe doping reduces both these resistances, while for deficient materials, Fe introduction does not improve the polarization resistance. Only a slight reduction of HF resistance is observed for NBCFd1 (Fe = 0.1) compared to NBCd (Fe = 0), but for Fe = 0.4 both MF and HF processes are more resistive than the other deficient compounds and NBCF4. The trends of resistance contributions are quite similar for HF and MF, and the main difference is evident for Fe content equal to 0.1. Regarding ion transfer at the cathode-electrolyte interface, NBCF1 shows remarkable improvement (7.4-fold reduction: from 2.77 $\Omega \cdot cm^2$ of NBC to 0.38 $\Omega \cdot cm^2$) compared to the smaller impact on surface electronation (2.5-fold reduction: from 12.12 to 4.80 $\Omega \cdot cm^2$). The reduction of the HF and MF resistances from NBC to NBCF4 shows instead comparable values (≈ 15-18 times).

The experimental results associated to Fe doping on the stoichiometric compounds support the outcomes of the theoretical simulations made by Anjum et al. [24], which show an increase of the oxygen diffusion in the crystal structure of $LnBa_{1-y}Sr_yCo_{2-x}Fe_xO_{5+\delta}$ (Ln = Pr, Gd, Nd) electrodes due to the introduction of 0.5 Fe doping. These authors also find that the improvement in diffusivity is restricted to the *a-b* plane, while it has a negligible effect in the *c* plane. The anisotropic diffusion for this class of ordered perovskite is well known and it is attributed to the regular alternation of the structure in double or layered perovskites compared to the simple perovskites [50-53]. A structural explanation of the increase of ionic diffusivity with the substitution of small amounts of Co with Fe is related to the increase of the unit cell volume, which results in a reduction in the strength of the Co-O bond [21]. However, for large degrees of Fe substitution, the activity dramatically drops due to the disappearance of oxygen vacancies in the structure and the shift to a disordered cubic perovskite structure [16, 18].
The oxygen ion diffusivity is a fundamental parameter in the ORR mechanism, but it is not trivial to derive its contribution in a single element with ECM technique. This is mainly due to the influence of this physical characteristic on different electrochemical steps of the ORR. In our ECM analyses, the resistance associated to oxygen lattice diffusion is included in the MF contribution. First, the characteristic frequencies of ionic transport in the lattice are in the MF range. A qualitative value of the frequency can be calculated as follows:

$$f \approx \frac{D_0}{d_{char}^2}$$

Where D_0 is the bulk diffusion coefficient and d_{char} is the characteristic length of the motion. Diffusion coefficients values are reported in literature in the range of 10^{-7}-10^{-6} cm^2/s at 700°C for $PrBaCo_{2-x}Fe_xO_{5+\delta}$ compounds [53-56]. Considering the microstructure observed in Fig. 3, the characteristic length can be assumed equal to 1 μm for the ionic diffusion in the bulk of a particle. Thus, the resistance contribution related to ion diffusion results in a characteristic frequency range of 10-100 Hz, in line with ECM estimates (Table 2). Furthermore, the MF contribution was found to be the most relevant step at all temperatures and O_2 conditions. Both the resistances and activation energies are higher than the HF process (Fig. 8), which indicates that the process at the cathodic surface governs the system kinetics, with a relatively fast oxygen diffusion above 650°C. However, decreasing the temperature, the arcs start showing a Gerischer-like shape at high frequencies. This is an indication that at low

temperature, the Adler-Steele-Lane (ASL) model could be more appropriate because it explicitly takes into account these ionic diffusivity limitations [57]. However, in order to be able to compare the parameters under all the conditions and extract the reaction orders, the EIS results were fitted only with one circuit, achieving satisfactory results.

The effect of Ba deficiency is found to be the opposite of Fe doping: it reduces the oxygen content and improves the activity of most of the perovskite compositions. The main effect of a deficiency on the crystal structures is both to introduce oxygen vacancies (as also evident by the results of oxygen titration of Fig. 2a and 2b) and increase the electron carriers (h•) in the lattice (Fig. 2c and 2d). The ratio between these two structural features is determined during the material synthesis by the charge compensation process, in order to maintain charge neutrality. The introduction of these defects usually improves the cathodic activity, but it requires an on optimization to achieve the best trade-off in terms of ORR activities [39]. This enhancement is attributed to an increase in both the oxygen surface exchange and the bulk diffusion rates and it is supported by our experimental results for Fe content of 0 and 0.1. An exception is represented by NBCF4, which presents a better activity than NBCFd4. A possible explanation of the opposite effect of Fe doping on stoichiometric and deficient materials is related to the position of the oxygen vacancies. Chen et al. [58] assumed that Ba deficiency introduces vacancies in the Ba-O layers due to the breaking of Ba-O bonds. This may enhance the oxygen ion diffusivity along the *c* axis and may shorten the oxygen diffusion length through the cathode lattice. Since ionic diffusion mainly occurs across *a*-*b* planes, its enhancement along the *c* axis can significantly improve the O^{2-} diffusion in a porous layer composed of randomly oriented grains. Typically, in $LnBaCo_2O_{5+\delta}$ materials, the oxygen vacancies are concentrated in the Ln-O layers, near cobalt ions with apical position in the Co-O octahedra. Increasing the vacancies leads some octahedra to lose an oxygen ion, reducing the oxidation state of cobalt and creating a preferential path for oxygen mobility. However, usually there exists an optimum in vacancies concentration. An excessive amount of vacancies is detrimental for ionic conduction due to the interaction between neighboring vacancies, which increases the activation energy of the charge mobility. The introduction of iron in the structure results in few octahedra with Fe cations instead of Co. The loss of the oxygen in Fe-O octahedra requires higher activation energy than in Co-O ones [36], becoming less favorable. This means that, upon increasing Fe doping, Co-O octahedra with full oxygen occupancy statistically increase and the distribution of oxygen vacancies becomes less homogenous. Therefore, the path will be more tangled due to random locations of full Fe-O octahedra distributed in the crystal structure. However, it is important to emphasize that many other parameters are involved in the oxygen reduction reaction, aside of oxygen diffusivity. The most relevant ORR step was found to be the electronation of the cathodic surface, meaning that the surface characteristics are decisive for the cathodic activity, especially due to compositional differences with the bulk of the material. The influence of the synthesis technique on the chemical surface exchange coefficient was demonstrated for the composition $PrBaCo_2O_{5+\delta}$ [44, 59, 60].

The variations of E_{ACT} in air (Fig. 8c) and capacitance at 600°C (Fig. 8d) are reported for all the samples of the NBCFd series. Concerning the effect of Fe doping on E_{ACT}, a clear difference is visible only for stoichiometric samples. NBCF2 and NBCF4 show a reduction of E_{ACT} compared to NBC and NBCF1, which is more evident for HF process. The effect of Ba

deficiency on the E_{ACT} of the HF process mirrors the evolution of the ASR, namely, a reduction for y = 0 and 0.1, and an increase for y = 0.4. On the contrary, the variation due to deficiency of the E_{ACT} for the MF step is almost negligible. This result is an indication of the different mechanisms of activity enhancements occurring due to Fe doping or Ba deficiency. Regarding HF and MF processes, the variations of the capacitances as a function of Fe doping are reversed compared to E_{ACT}. Instead, the effects of Ba deficiency on the capacitance are analogous to those observed for E_{ACT}. In particular, both Fe doping and Ba deficiency influence the values but do not further modify the capacitances, when introduced simultaneously. The significant variations of these values indicate that the morphological features change due to the compositional tailoring of the compounds. This result evidences the key-role played by the surface in the global mechanism of cathode reaction.

Conclusions

The effects of Fe doping (up to 20%) and Ba deficiency (up to 10%) on crystal structure, oxygen reduction behavior and electrochemical properties of $NdBa_{1-x}Co_{2-y}Fe_yO_{5+\delta}$ (NBCFd) layered perovskites are investigated. The compounds crystallize in an ordered layered structure with tetragonal lattice (*P4/mmm*), whose cell volume increases with Fe doping, both in stoichiometric samples and in Ba deficient ones. The introduction of Ba deficiency affects the cell size in the opposite way, slightly decreasing lattice parameters. The entire series shows high total conductivity (between 150 and 450 S/cm at 700°C), despite increasing Fe doping reduces the global conductivity. In stoichiometric compounds, the polarization resistances benefit from the introduction of Fe, while they increase for compounds with Ba deficiency. The best performance is obtained at 10% Fe doping and 5% Ba deficiency (0.14 $\Omega \cdot cm^2$ at 700°C), which allows to meet the requirement for application as IT-SOFC cathode. Detailed ECM analysis on the results of EIS tests at varying temperature (550 to 700°C) and O_2 content (100% to 5% v/v) reveals that the main step in terms of polarization resistance is the surface electronation of adsorbed oxygen. The secondary step of the process is associated to the transfer of oxide ions across the interface between cathode and electrolyte. Based on DRT and ECM analyses, the effects of Fe doping and Ba deficiency on the ORR mechanism are evaluated: Fe doping promotes electronation and ion transfer in Ba stoichiometric compounds but hampers the electronation when Ba is deficient. This indicates that distinct and contrasting mechanisms of activity enhancement occur due to the compositional tailoring.

References

1. R. Pelosato, G. Cordaro, D. Stucchi, C. Cristiani, and G. Dotelli, *J. Power Sources,* **298** 46-67 (2015).
2. S. Afroze, A. Karim, Q. Cheok, S. Eriksson, and A. K. Azad, *Frontiers in Energy,* (2019).
3. A. Subardi, K.-Y. Liao, and Y.-P. Fu, *J. Eur. Ceram. Soc.,* **39** (1), 30-40 (2019).
4. X. Zhu, C. Qian, F. Sun, L. Zhang, X. Liu, and D. Li, *J. Alloys Compd.,* **802** 415-421 (2019).
5. S. Pang, Y. Su, G. Yang, X. Shen, M. Zhu, X. Wu, S. Li, X. Yang, and X. Xi, *Ceram. Int.,* **44** (17), 21902-21907 (2018).
6. C. Yao, H. Zhang, X. Liu, J. Meng, X. Zhang, F. Meng, and J. Meng, *Ceram. Int.,* **44** (11), 12048-12054 (2018).
7. J. Chen, J. Li, L. Jia, I. Moussa, B. Chi, J. Pu, and J. Li, *J. Power Sources,* **428** 13-19 (2019).
8. A. Olszewska, K. Świerczek, W. Skubida, Z. Du, H. Zhao, and B. Dabrowski, *The Journal of Physical Chemistry C,* **123** (1), 48-61 (2019).
9. C. Sun, Y. Kong, L. Shao, Q. Zhang, X. Wu, N. Zhang, and K. Sun, *ACS Sustainable Chemistry & Engineering,* **7** (13), 11603-11611 (2019).
10. J. Wang, F. Meng, T. Xia, Z. Shi, J. Lian, C. Xu, H. Zhao, J.-M. Bassat, and J.-C. Grenier, *Int. J. Hydrogen Energy,* **39** (32), 18392-18404 (2014).
11. X. Jiang, Q. Xu, Y. Shi, X. Li, W. Zhou, H. Xu, and Q. Zhang, *Int. J. Hydrogen Energy,* **39** (21), 10817-10823 (2014).
12. S. Pang, X. Jiang, X. Li, Q. Wang, and Z. Su, *J. Power Sources,* **204** 53-59 (2012).
13. X. Ding, Z. Gao, D. Ding, X. Zhao, H. Hou, S. Zhang, and G. Yuan, *Applied Catalysis B: Environmental,* **243** 546-555 (2019).
14. K. Yi, L. Sun, Q. Li, T. Xia, L. Huo, H. Zhao, J. Li, Z. Lü, J.-M. Bassat, A. Rougier, S. Fourcade, and J.-C. Grenier, *Int. J. Hydrogen Energy,* **41** (24), 10228-10238 (2016).
15. A. Donazzi, R. Pelosato, G. Cordaro, D. Stucchi, C. Cristiani, G. Dotelli, and I. N. Sora, *Electrochim. Acta,* **182** 573-587 (2015).
16. V. A. Cherepanov, T. V. Aksenova, L. Y. Gavrilova, and K. N. Mikhaleva, *Solid State Ionics,* **188** (1), 53-57 (2011).
17. L. Jiang, T. Wei, R. Zeng, W.-X. Zhang, and Y.-H. Huang, *J. Power Sources,* **232** 279-285 (2013).
18. Y. N. Kim, J. H. Kim, and A. Manthiram, *J. Power Sources,* **195** (19), 6411-6419 (2010).
19. D. S. Tsvetkov, I. L. Ivanov, and A. Y. Zuev, *J. Solid State Chem.,* **199** 154-159 (2013).
20. J. Xue, Y. Shen, and T. He, *J. Power Sources,* **196** (8), 3729-3735 (2011).
21. L. Zhao, J. Shen, B. He, F. Chen, and C. Xia, *Int. J. Hydrogen Energy,* **36** (5), 3658-3665 (2011).
22. S.-L. Zhang, K. Chen, A.-P. Zhang, C.-X. Li, and C.-J. Li, *Ceram. Int.,* **43** (15), 11648-11655 (2017).
23. J. Zou, J. Park, B. Kwak, H. Yoon, and J. Chung, *Solid State Ionics,* **206** 112-119 (2012).
24. U. Anjum, S. Vashishtha, N. Sinha, and M. A. Haider, *Solid State Ionics,* **280** 24-29 (2015).
25. A. C. Larson and R. B. Von Dreele, *Los Alamos National Laboratory Report LAUR,* 86-748 (2000).
26. J. Wright and A. V. Virkar, *J. Power Sources,* **196** (15), 6118-6124 (2011).
27. M. Saccoccio, T. H. Wan, C. Chen, and F. Ciucci, *Electrochim. Acta,* **147** 470-482 (2014).
28. G. Cordaro, A. Donazzi, R. Pelosato, C. Cristiani, G. Dotelli, and I. Natali Sora, *ECS Transactions,* **78** (1), 507-520 (2017).
29. R. D. Shannon, *Acta Crystallogr.,* **32A** (2), 751-767 (1976).
30. F. Jin, Y. Shen, R. Wang, and T. He, *J. Power Sources,* **234** 244-251 (2013).
31. F. Jin, H. Xu, W. Long, Y. Shen, and T. He, *J. Power Sources,* **243** 10-18 (2013).

32. R. A. Cox-Galhotra, A. Huq, J. P. Hodges, J.-H. Kim, C. Yu, X. Wang, A. J. Jacobson, and S. McIntosh, *Journal of Materials Chemistry A,* **1** (9), 3091 (2013).
33. F. A. Kröger and H. J. Vink, *Solid State Physics,* **3** 307-435 (1956).
34. N. E. Volkova, L. Y. Gavrilova, V. A. Cherepanov, T. V. Aksenova, V. A. Kolotygin, and V. V. Kharton, *J. Solid State Chem.,* **204** 219-223 (2013).
35. X. Mao, T. Yu, and G. Ma, *J. Alloys Compd.,* **637** 286-290 (2015).
36. S. Choi, S. Yoo, J. Kim, S. Park, A. Jun, S. Sengodan, J. Kim, J. Shin, H. Y. Jeong, Y. Choi, G. Kim, and M. Liu, *Scientific Reports,* **3** 1-6 (2013).
37. B. C. H. Steele, *Solid State Ionics,* **134** 3-20 (2000).
38. N. S. Tsvetkova, A. Y. Zuev, and D. S. Tsvetkov, *J. Power Sources,* **243** 403-408 (2013).
39. S. B. Adler, *Chem. Rev.,* **104** 4791-4843 (2004).
40. B. A. Boukamp and A. Rolle, *Solid State Ionics,* **314** 103-111 (2018).
41. A. Bertei, E. Ruiz-Trejo, F. Tariq, V. Yufit, A. Atkinson, and N. P. Brandon, *Int. J. Hydrogen Energy,* **41** (47), 22381-22393 (2016).
42. F. Ciucci, *Current Opinion in Electrochemistry,* **13** 132-139 (2019).
43. Z. Shi, T. Xia, F. Meng, J. Wang, J. Lian, H. Zhao, J. M. Bassat, J. C. Grenier, and J. Meng, *Fuel Cells,* **14** (6), 979-990 (2014).
44. S. Pang, W. Wang, T. Chen, Y. Wang, K. Xu, X. Shen, X. Xi, and J. Fan, *Int. J. Hydrogen Energy,* **41** (31), 13705-13714 (2016).
45. D. Chen, R. Ran, K. Zhang, J. Wang, and Z. Shao, *J. Power Sources,* **188** (1), 96-105 (2009).
46. S. Pang, X. Jiang, X. Li, Q. Wang, Z. Su, and Q. Zhang, *Int. J. Hydrogen Energy,* **37** (5), 3998-4001 (2012).
47. R. Pelosato, A. Donazzi, G. Dotelli, C. Cristiani, I. Natali Sora, and M. Mariani, *J. Eur. Ceram. Soc.,* **34** (16), 4257-4272 (2014).
48. Y. Takeda, R. Kanno, M. Noda, Y. Tomida, and O. Yamamoto, *J. Electrochem. Soc.,* **134** (11), 2656-2661 (1987).
49. S. Li, T. Xia, Q. Li, L. Sun, L. Huo, and H. Zhao, *Int. J. Hydrogen Energy,* **42** (38), 24412-24425 (2017).
50. A. Maignan, C. Martin, D. Pelloquin, N. Nguyen, and B. Raveau, *J. Solid State Chem.,* **142** 247-260 (1999).
51. A. A. Taskin, A. N. Lavrov, and Y. Ando, *Appl. Phys. Lett.,* **86** (9), 091910 (2005).
52. D. Parfitt, A. Chroneos, A. Tarancón, and J. A. Kilner, *J. Mater. Chem.,* **21** (7), 2183 (2011).
53. M. Burriel, J. Peña-Martínez, R. J. Chater, S. Fearn, A. V. Berenov, S. J. Skinner, and J. A. Kilner, *Chem. Mater.,* **24** (3), 613-621 (2012).
54. F. Dong, M. Ni, Y. Chen, D. Chen, O. M. Tadé, and Z. Shao, *Journal of Materials Chemistry A,* **2** (48), 20417-21022 (2014).
55. A. Grimaud, J. M. Bassat, F. Mauvy, M. Pollet, A. Wattiaux, M. Marrony, and J. C. Grenier, *Journal of Materials Chemistry A,* **2** (10), (2014).
56. G. Kim, S. Wang, A. J. Jacobson, L. Reimus, P. Brodersen, and C. A. Mims, *J. Mater. Chem.,* **17** (24), 2500 (2007).
57. S. B. Adler, J. A. Lane, and B. C. H. Steele, *J. Electrochem. Soc.,* **143** (11), 3554-3564 (1996).
58. T. Chen, S. Pang, X. Shen, X. Jiang, and W. Wang, *RSC Advances,* **6** (17), 13829-13836 (2016).
59. R. A. Cox-Galhotra and S. McIntosh, *Solid State Ionics,* **228** 14-18 (2012).
60. J. Liu, G. Collins, M. Liu, C. Chen, J. He, J. Jiang, and E. I. Meletis, *Appl. Phys. Lett.,* **100** (19),

193903 (2012).

Tables

Table 1. List of NBCFd sample names with oxygen contents, measured by titrations, and crystallographic information, such as space group and cell parameters obtained by Rietveld refinement.

Sample	Formula	Space Group	a [Å]	b [Å]	c [Å]	V [Å^3]	5+δ	Ref.
NBC[1]	$NdBaCo_2O_{5+\delta}$	*Pmmm*	3.89921(9)	7.8107(2)	7.6125(1)	115.92[1]	5.64	15
NBCF1	$NdBaCo_{1.9}Fe_{0.1}O_{5+\delta}$	*P4/mmm*	3.90017(7)	-	7.6148(2)	115.831(5)	5.63	This Work
NBCF2	$NdBaCo_{1.8}Fe_{0.2}O_{5+\delta}$	*P4/mmm*	3.90335(6)	-	7.6268(2)	116.204(5)	5.64	This Work
NBCF3	$NdBaCo_{1.7}Fe_{0.3}O_{5+\delta}$	*P4/mmm*	3.90307(7)	-	7.6290(2)	116.220(5)	5.67	This Work
NBCF4	$NdBaCo_{1.6}Fe_{0.4}O_{5+\delta}$	*P4/mmm*	3.90520(6)	-	7.6454(2)	116.596(4)	5.71	This Work
NBCd	$NdBa_{0.9}Co_2O_{5+\delta}$	*P4/mmm*	3.89858(4)	-	7.6113(1)	115.683(3)	5.60	15
NBCFd1	$NdBa_{0.9}Co_{1.9}Fe_{0.1}O_{5+\delta}$	*P4/mmm*	3.89690(8)	-	7.6144(3)	115.631(5)	5.52	This Work
NBCFd4	$NdBa_{0.9}Co_{1.6}Fe_{0.4}O_{5+\delta}$	*P4/mmm*	3.90220(1)	-	7.6503(3)	116.494(7)	5.56	This Work

[1] Refined in an orthorhombic doubled unit cell $a_p \times 2a_p \times 2a_p$; the reported volume is the reduced cell volume calculated for an $a_p \times a_p \times 2a_p$ cell for comparison with other samples. a_p is the lattice parameter of the cubic perovskite.

Table 2. ECM fitting parameters for the NBCFd1 sample in air at different temperature.

Element	700°C	650°C	600°C	550°C	Unit
L	6.4E-07	4.2E-07	4.2E-07	1.4E-06	[H]
R_{Ohm}	1.689	2.560	4.150	7.215	[Ω·cm^2]
R_{HF}	0.036	0.077	0.160	0.480	[Ω·cm^2]
QPE_{HF}-Q	1.55E-02	1.20E-02	1.10E-02	8.00E-03	[F/cm^2]
QPE_{HF}-n	0.780	0.760	0.740	0.740	[-]
C_{HF}	2.76E-03	1.32E-03	1.18E-03	1.13E-03	[F/cm^2]
f_{HF}	1.61E+03	1.57E+03	8.40E+02	2.93E+02	[Hz]
R_{MF}	0.086	0.214	0.490	1.315	[Ω·cm^2]
QPE_{MF}-Q	4.70E-02	5.20E-02	4.97E-02	4.20E-02	[F/cm^2]
QPE_{MF}-n	0.85	0.820	0.816	0.810	[-]
C_{MF}	1.78E-02	1.94E-02	2.15E-02	2.13E-02	[F/cm^2]
f_{MF}	1.04E+02	3.83E+01	1.51E+01	5.68E+00	[Hz]
R_{LF}	0.017	0.020	0.021	0.022	[Ω·cm^2]
QPE_{LF}-Q	2.57E+00	5.75E+00	8.75E+00	1.95E+01	[F/cm^2]
QPE_{LF}-n	0.983	0.983	0.983	0.983	[-]
C_{LF}	2.44E+00	5.54E+00	8.50E+00	1.92E+01	[F/cm^2]
f_{LF}	3.77E+00	1.44E+00	8.85E-01	3.86E-01	[Hz]

706 **Table 3.** ECM fitting parameters for the NBCFd1 sample at 700°C at different oxygen partial pressure.

Element	100%	21%	10%	5%	Unit
L	5.74E-07	6.43E-07	5.85E-07	5.66E-07	[H]
R_{Ohm}	1.69	1.69	1.70	1.70	[Ω·cm^2]
R_{HF}	0.034	0.036	0.039	0.040	[Ω·cm^2]
QPE_{HF}-Q	2.60E-02	1.56E-02	3.03E-02	2.99E-02	[F/cm^2]
QPE_{HF}-n	0.750	0.780	0.760	0.760	[-]
C_{HF}	2.50E-03	2.76E-03	3.59E-03	3.57E-03	[F/cm^2]
f_{HF}	1.88E+03	1.61E+03	1.14E+03	1.12E+03	[Hz]
R_{MF}	0.055	0.086	0.103	0.124	[Ω·cm^2]
QPE_{MF}-Q	6.56E-02	4.70E-02	6.44E-02	6.28E-02	[F/cm^2]
QPE_{MF}-n	0.80	0.85	0.82	0.86	[-]
C_{MF}	1.61E-02	1.78E-02	2.14E-02	2.85E-02	[F/cm^2]
f_{MF}	1.80E+02	1.04E+02	7.19E+01	4.50E+01	[Hz]
R_{LF}	\	0.017	0.034	0.077	[Ω·cm^2]
QPE_{LF}-Q	\	2.57E+00	3.11E+00	3.53E+00	[F/cm^2]
QPE_{LF}-n	\	0.98	0.98	0.90	[-]
C_{LF}	\	2.44E+00	2.99E+00	3.06E+00	[F/cm^2]
f_{LF}	\	3.77E+00	1.57E+00	6.77E-01	[Hz]

707

708

Figure Captions

Figure 1. XRPD patterns for all the compounds of the NBCFd series. NBC and NBCd measurements are taken from reference [15]. Peaks of impurity phases are marked with ♦ for $NdCoO_3$ (PDF #00-025-1064), ♣ for $BaCoO_{2.93}$ (PDF #00-026-0144) and ♠ for Nd_2O_3 (PDF #00-006-0408).

Figure 2. TGA and total conductivity measurements for the NBCFd samples. Oxygen content as a function of temperature under airflow for stoichiometric (Panel a) and deficient compounds (Panel b). Heating ramp rate of 3°C/min. Conductivity as a function of temperature for stoichiometric (Panel c) and deficient compounds (Panel d). The measurements for the NBC and NBCd samples are taken from reference [15].

Figure 3. SEM image of the cathodic porous layer of NBCFd1 deposited on a GDC dense pellet. Panel a reports the cross section of the electrode above the electrolyte and Panel b shows the top surface of the electrode.

Figure 4. Arrhenius plots of the ASR for the stoichiometric (Panel a) and deficient compounds (Panel b) of the NBCFd series. Panel c reports the ASR values at 600°C in air as a function of Fe content for stoichiometric (red circles) and deficient compounds (blue squares). Panel d reports the activation energies calculated for the ASR in air. The results of iron free compounds (NBC and NBCd) are taken from reference [15].

Figure 5. Nyquist plots for the sample NBCFd1/GDC/NBCFd1 with symmetric configuration. The measurements are collected at OCV, under different oxygen partial pressure in N_2, in the 10 kHz-0.1 Hz frequency range, from 700°C to 550°C. Panel a reports also the test performed in 5% O_2 in He. Circles are experimental data and numbers near filled circles represent the logarithm of the frequency decade. Lines represent the results of fitting with ECM technique and the used model is reported in Panel a.

Figure 6. Distribution of Relaxation Time (DRT) results for NBCFd1 sample for every temperature varying the oxygen content.

Figure 7. Resistance contributions of the NBCFd1 sample as a function of the oxygen partial pressure for high frequency (R_{HF}, Panel a), middle frequency (R_{MF}, Panel b), low frequency (R_{LF}, Panel c). Arrhenius plot of the resistance of the high frequency (HF), middle frequency (MF) and low frequency (LF) processes under air flow (Panel d).

Figure 8. Polarization resistance as a function of Fe content for high frequency (Panel a) and middle frequency contributions (Panel b) for stoichiometric (blue squares) and deficient compounds (red circles). Variation of E_{ACT} (Panel c) and capacitance at 600°C (Panel d) of the HF (full circles) and MF (half

753 squares) contributions for stoichiometric (blue) and deficient compounds (red). The results of iron free
754 compounds (NBC and NBCd) are taken from reference [15].
755
756

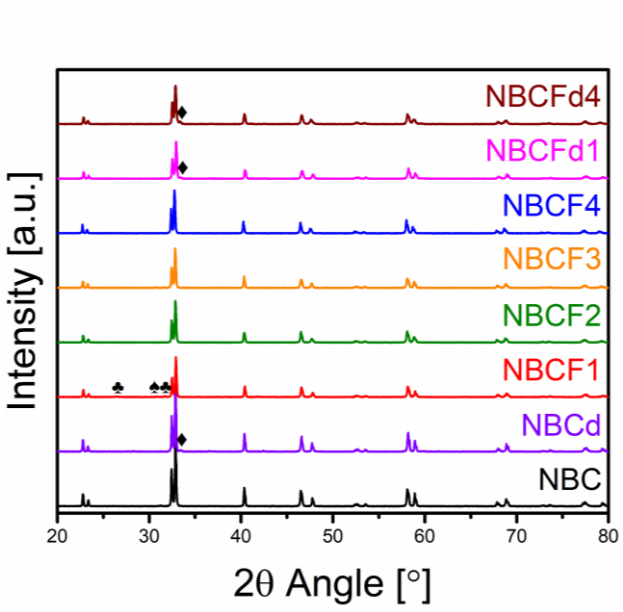
NBCFd4
NBCFd1
NBCF4
NBCF3
NBCF2
NBCF1
NBCd
NBC
Intensity [a.u.]
20
30
40
50
60
70
80
2θ Angle [°]

Figure 1.

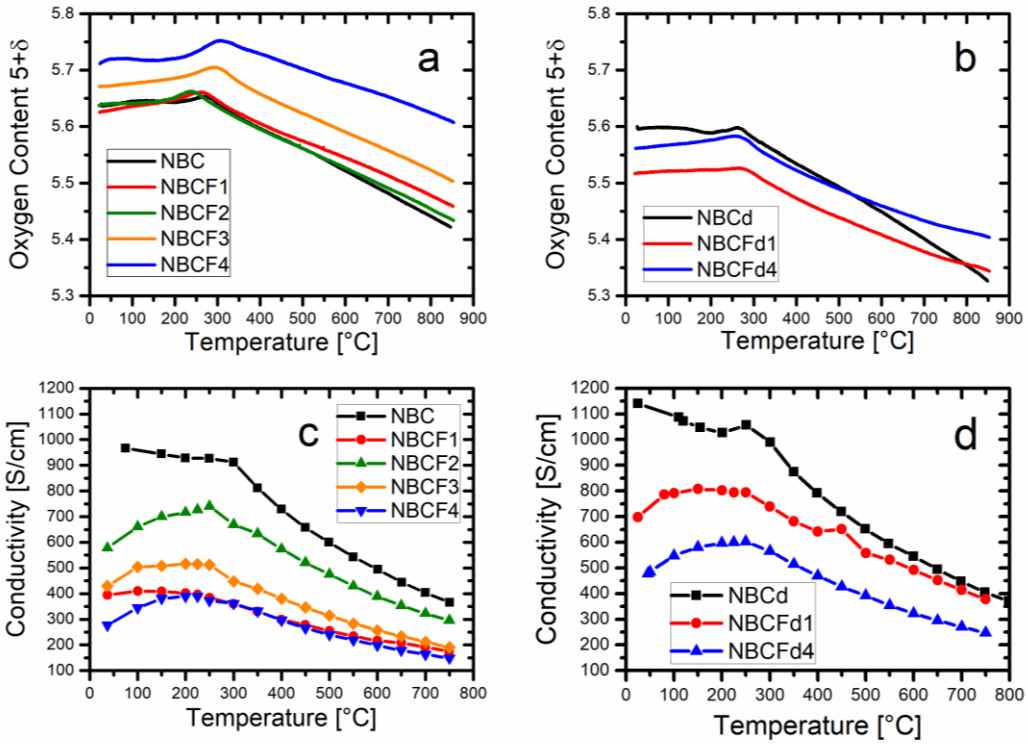
a
Oxygen Content 5+δ
Temperature [°C]
NBC
NBCF1
NBCF2
NBCF3
NBCF4
b
Oxygen Content 5+δ
Temperature [°C]
NBCd
NBCFd1
NBCFd4
c
Conductivity [S/cm]
Temperature [°C]
NBC
NBCF1
NBCF2
NBCF3
NBCF4
d
Conductivity [S/cm]
Temperature [°C]
NBCd
NBCFd1
NBCFd4

Figure 2.

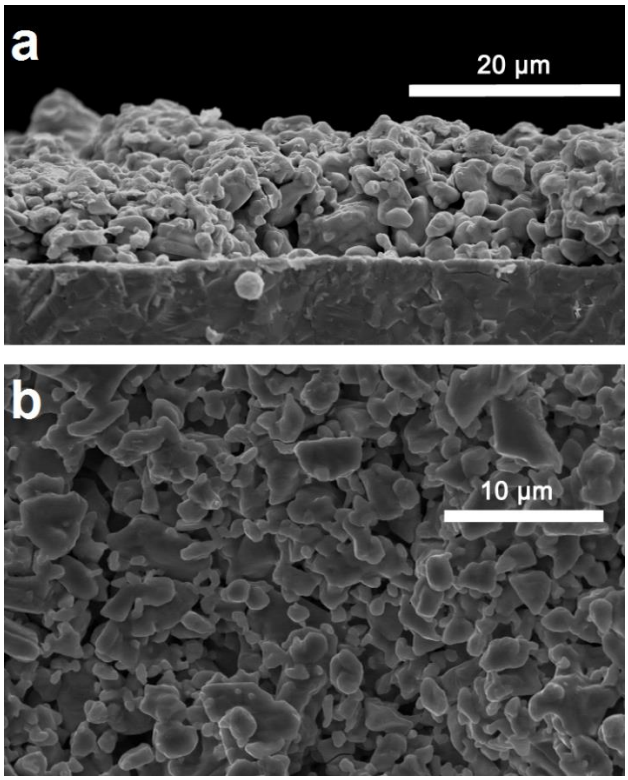

Figure 3.

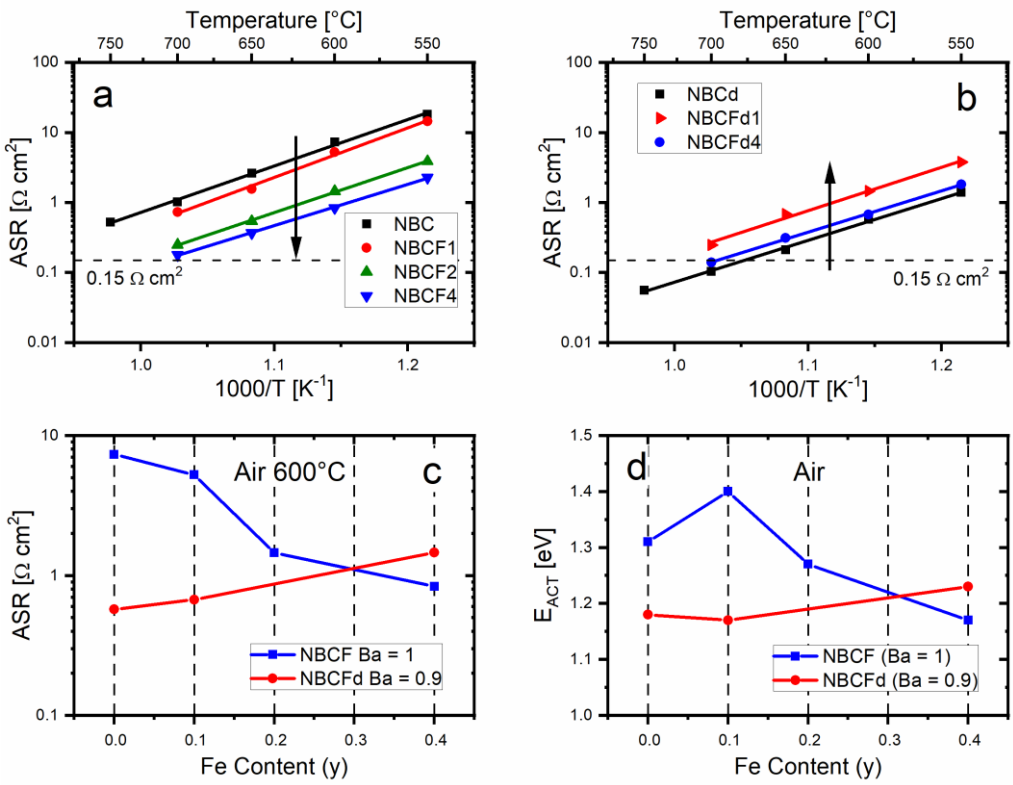
Temperature [°C]
750
700
650
600
550
100
10
1
0.1
0.01
a
ASR [Ω cm²]
0.15 Ω cm²
NBC
NBCF1
NBCF2
NBCF4
1.0
1.1
1.2
1000/T [K⁻¹]
b
NBCd
NBCFd1
NBCFd4
c
Air 600°C
NBCF Ba = 1
NBCFd Ba = 0.9
Fe Content (y)
d
Air
E_ACT [eV]
NBCF (Ba = 1)
NBCFd (Ba = 0.9)

Figure 4.

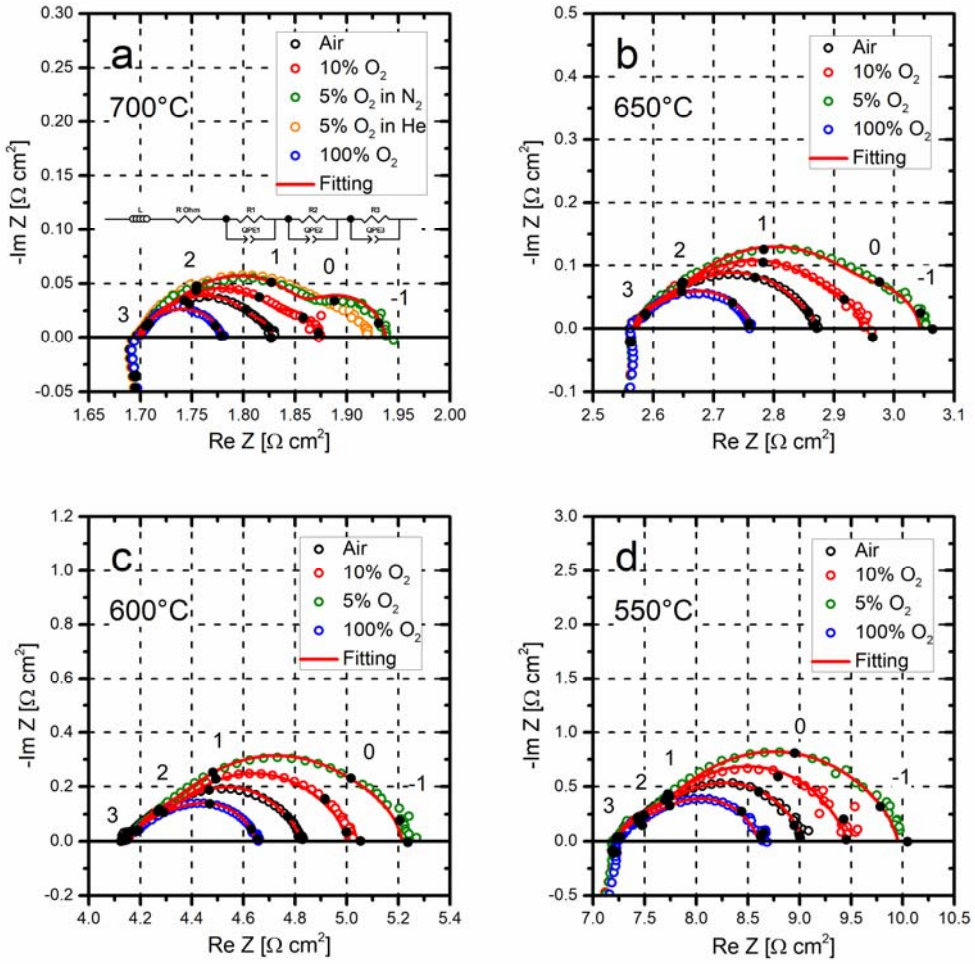
a
700°C
Air
10% O2
5% O2 in N2
5% O2 in He
100% O2
Fitting
b
650°C
c
600°C
d
550°C
-Im Z [Ω cm2]
Re Z [Ω cm2]

Figure 5.

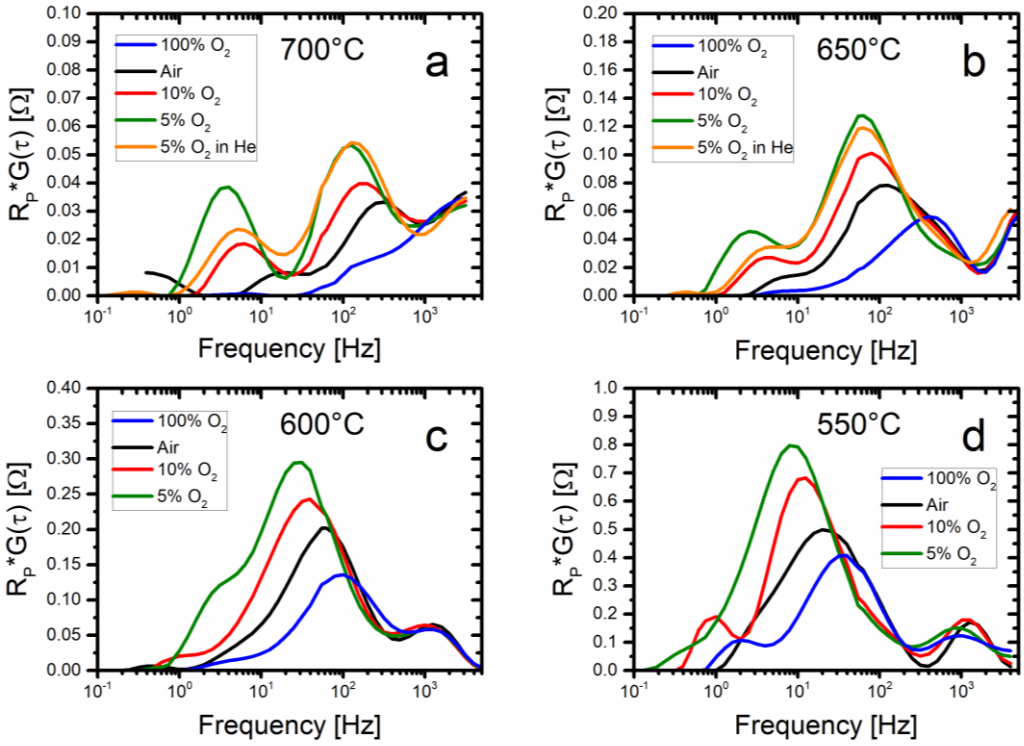
700°C
a
650°C
b
600°C
c
550°C
d
100% O2
Air
10% O2
5% O2
5% O2 in He
RP*G(τ) [Ω]
Frequency [Hz]

Figure 6.

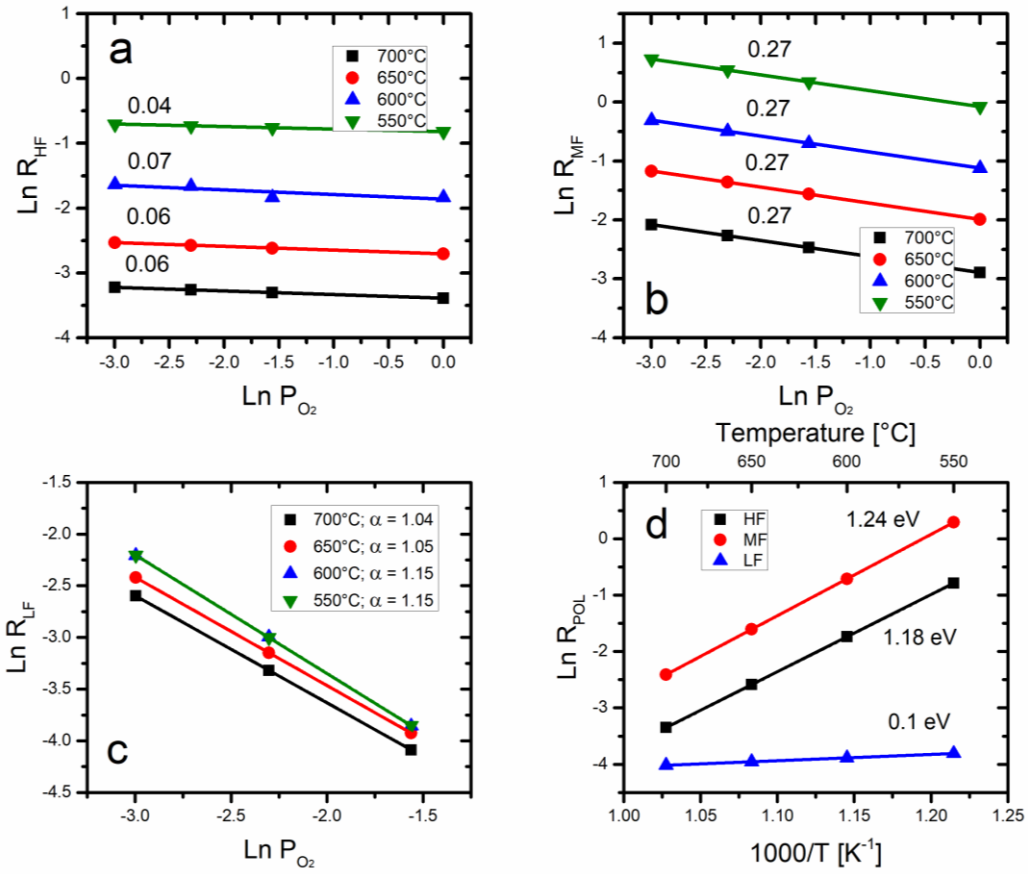
a
700°C
650°C
600°C
550°C
0.04
0.07
0.06
0.06
Ln R_HF
Ln P_O2
b
0.27
0.27
0.27
0.27
Ln R_MF
Ln P_O2
Temperature [°C]
700
650
600
550
c
700°C; α = 1.04
650°C; α = 1.05
600°C; α = 1.15
550°C; α = 1.15
Ln R_LF
Ln P_O2
d
HF
MF
LF
1.24 eV
1.18 eV
0.1 eV
Ln R_POL
1000/T [K^-1]

Figure 7.

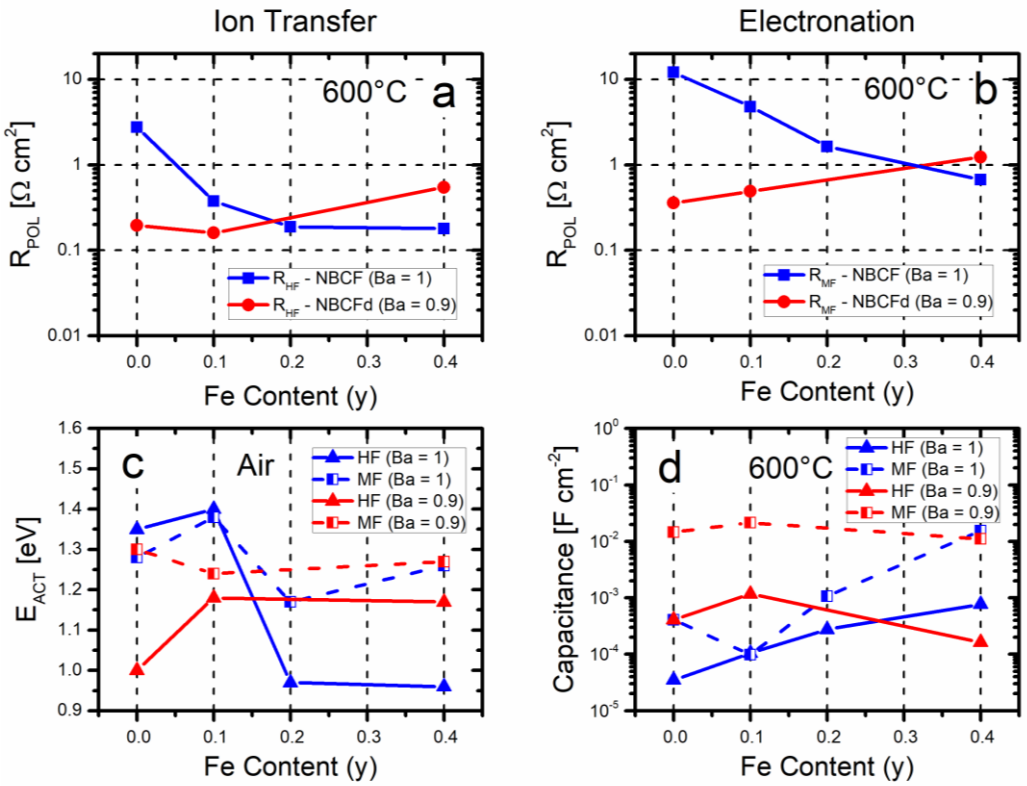
Ion Transfer
Electronation
600°C a
600°C b
R_{POL} [Ω cm^2]
R_{HF} - NBCF (Ba = 1)
R_{HF} - NBCFd (Ba = 0.9)
R_{MF} - NBCF (Ba = 1)
R_{MF} - NBCFd (Ba = 0.9)
Fe Content (y)
c Air
d 600°C
E_{ACT} [eV]
Capacitance [F cm^{-2}]
HF (Ba = 1)
MF (Ba = 1)
HF (Ba = 0.9)
MF (Ba = 0.9)

Figure 8.